HHS Public Access

Author manuscript

Nat Biotechnol. Author manuscript; available in PMC 2019 May 26.

An oncolytic herpes virus expressing E-cadherin resists NK cell clearance and improves viral spread and glioblastoma virotherapy

Bo Xu[#1,2,3], **Rui Ma**[#2], **Luke Russell**[2], **Ji Young Yoo**[4], **Jianfeng Han**[2], **Hanwei Cui**[2,3], **Ping Yi**[3], **Jianying Zhang**[5], **Hiroshi Nakashima**[6], **Hongsheng Dai**[2], **E. Antonio Chiocca**[6], **Balveen Kaur**[4], **Michael A Caligiuri**[7,8], and **Jianhua Yu**[1,2,7,8,*]

[1]Department of Internal Medicine, Division of Hematology, College of Medicine, The Ohio State University, Columbus, Ohio 43210, USA

[2]The Ohio State University Comprehensive Cancer Center, Columbus, Ohio 43210, USA

[3]Third Affiliated Hospital, Army Medical University, Chongqing 400042, China

[4]Department of Neurosurgery, The Vivian L. Smith University of Texas, University of Texas Health Science Center at Houston, Houston, TX 77030, USA

[5]Department of Information Sciences, Division of Biostatistics, City of Hope National Medical Center, Duarte, CA 91010

[6]Department of Neurosurgery, Brigham and Women's Hospital and Harvey Cushing Neuro-oncology Laboratories, Harvard Medical School, Boston, Massachusetts 02115, USA

[7]Hematologic Malignancies and Stem Cell Transplantation Institute, City of Hope National Medical Center, Duarte, California 91010, USA

[8]Department of Hematology & Hematopoietic Cell Transplantation, City of Hope National Medical Center, Duarte, California 91010, USA

[#] These authors contributed equally to this work.

Editor Summary:

[*]Corresponding author. jiayu@coh.org.

Authorship Contribution:

B.X. performed experiments, designed research and wrote the manuscript; R.M., L.R., J.Y.Y. and J.H., H.C., and P.Y. performed experiments; H.D. designed research; J.Z. analyzed the data; H.N. provided materials; E.A.C. and B.K. designed research and reviewed the manuscript; M.A.C. designed research, reviewed and edited the manuscript and acquired funding. J.Y. designed research, wrote the manuscript, acquired funding and supervised the study.

Ethics statement:

Experiments and handling of mice were conducted under federal, state and local guidelines and with an approval from the Ohio State University Institutional Animal Care and Use Committee.

Data availability statement.

All summary or representative data generated and supporting the findings of this study are available within the paper. Raw data that support the findings of this study are available upon request.

Conflict-of-interest disclosure:

A patent application on OV-CDH1 virus related to this work has recently been submitted by The Ohio State University on behalf of the inventors, J.Y, M.A.C and B.X. Other authors declare no conflict of interest.

An engineered oncolytic herpes virus shows enhanced intratumoral spread, resistance to NK cell clearance and improved efficacy against brain cancer in mice.

Life Sciences Reporting Summary:

Further information on experimental design is available in the Nature Research Reporting Summary.

The efficacy of oncolytic herpes simplex virus (oHSV) is limited by rapid viral clearance by innate immune effector cells and poor intratumoral viral spread. We combine two approaches to overcome these barriers—inhibition of natural killer (NK) cells and enhancement of intratumoral viral spread. We engineered an oHSV to express E-cadherin (E-cad), an adherent molecule and a ligand for KLRG1, an inhibitory receptor expressed on NK cells. *In vitro*, infection with this engineered virus, named OV-CDH1, induces high surface E-cad expression on infected glioblastoma (GBM) cells, which typically lack endogenous E-cad. Ectopically expressed E-cad enhances the spread of OV-CDH1 by facilitating cell-to-cell infection and viral entry and reduces viral clearance by selectively protecting OV-CDH1-infected cells from $KLRG1^+$ NK cell killing, while NK cell anti-tumor activity is largely preserved. *In vivo,* OV-CDH1 treatment substantially prolongs the survival in GBM-bearing mouse models. Thus, virus-induced overexpression of E-cad may be a generalizable strategy for improving cancer virotherapy.

Oncolytic herpes simplex virus (oHSV) has shown efficacy in treating such cancers as glioblastoma (GBM), melanoma, breast cancer and ovarian cancer[1–4]. In 2015, the FDA approved the first oHSV, Imlygic (talimogene laherparepvec), for melanoma treatment[5]. However, the anti-tumor efficacy of oHSV is diminished in two key ways. First, the host antiviral innate immune response to oHSV infection impairs efficient viral replication and propagation within tumors[6–8]. Second, intratumoral spread of oHSV is limited by several factors, including the extracellular matrix and areas of fibrosis and necrosis[9]. Previous studies have demonstrated that systemic depletion or inhibition of natural killer (NK) cells significantly improves the efficacy of oHSV treatment for GBM[6–8, 10], although the antitumor effect of NK cells is also impaired. Other work has shown that enhancing viral spread improves the efficacy of oHSV[11–13]. We hypothesized that combining the two strategies could further boost oHSV efficacy, and we aimed to achieve both effects by engineering oHSV to express a molecule that simultaneously blocks cytolytic NK cell activity and promotes viral infectivity.

We focused on the inhibitory signaling through killer cell lectin-like receptor G1 (KLRG1), an inhibitory receptor expressed by NK cells and activated T cells. Human E-cadherin (E-cad) binding to human or murine KLRG1 protects E-cad-expressing cells from being lysed by human or mouse NK cells[14–16]. Compared to systematic inhibition or depletion of NK cells, overexpressing E-cad on viral infected cells selectively protects oHSV-infected cells from those NK cells that interact with virus-infected cells but anti-tumor activity of most other NK cells remains. Moreover, E-cad is also a calcium-dependent cell-cell adhesion molecule that cooperates with nectin-1 in the formation of cell-cell adherens junctions[17, 18]. Nectin-1 is crucial for HSV-1 infection, and the binding of nectin-1 to HSV-1 glycoprotein

D (gD) triggers the viral entry of HSV[19]. Overexpressing E-cad on the virus-infected cells may directly facilitate the cell-to-cell infection, which is the dominant way of intratumoral viral spread, while without modification of viral glycoproteins, this approach avoids the change on viral tropism.

We generated an oHSV, called OV-CDH1, by incorporating human *CDH1,* encoding E-cad, into the parental oHSV genome. We then tested the anti-tumor efficacy of OV-CDH1 against GBM. GBM is the most common primary brain malignancy and is in urgent need of more effective therapeutics[20]. Our results show that E-cad overexpression inhibited the antiviral activity of NK cells, facilitated cell-to-cell viral infection and accelerated the viral entry. Studies with both xenograft and immunocompetent mouse models of GBM demonstrate that OV-CDH1 leads to enhanced survival compared with parental oHSV. When combined with NK cell depletion, OV-CDH1 still outperforms analogous combinatorial treatment with parental oHSV, suggesting that enhanced viral spread likely plays a larger role than NK cell inhibition in improving the efficacy of OV-CDH1.

Results

E-cadherin expression on GBM cells after OV-CDH1 infection

We generated an oHSV (OV-CDH1), that carries a human E-cadherin (E-cad) coding gene (*CDH1*) driven by the HSV-1 immediate early gene promoter pIE4/5. The parental oHSV, is double-attenuated, with an inactivated ribonucleotide reductase gene (ICP6), and deletions of both copies of the neurovirulence gene (ICP34.5) (Supplementary Fig. 1a)[21]. These genetic disruptions result in (a) selective viral replication in tumor cells, as proliferating tumor cells compensate for the loss of ICP6 with host ribonucleotide reductase, which is not present in normal cells, and (b) a reduction in neurovirulence[22]. The FDA-approved oHSV Imlygic shares a similar backbone[5]. To characterize the role of the extracellular domain of E-cad, we also generated a mutant version of OV-CDH1 (OV-IL2RA-CDH1), in which the extracellular domain of E-cad was replaced with that of the interleukin-2 receptor alpha chain (IL2RA)[23]. The genetic maps of wild-type human HSV-1, parental oHSV (OV-Q1), OV-CDH1 and OV-IL2RA-CDH1 are shown in Supplementary Figure 1a. OV-CDH1 and OV-IL2RA-CDH1 infections induced E-cad and IL2RA/E-cad expression on GBM cells, respectively (Supplementary Note 1, Supplementary Fig. 1b,c,d,e,f).

Resistance of OV-CDH1-infected GBM cells to NK cell clearance

Given our previous findings[7, 8], we next tested the sensitivity of OV-CDH1-infected GBM cells to NK cell-mediated killing. Both OV-Q1 and OV-CDH1 infections increased the susceptibility of GBM cells to NK cell cytotoxicity (Fig. 1a). However, compared to OV-Q1-infected cells, fewer OV-CDH1-infected cells were killed when co-cultured with bulk human primary NK cells (approximately 50% $KLRG1^+$) (Fig. 1a; Supplementary Fig. 2). Notably, the inhibitory effect was completely abolished with OV-IL2RA-CDH1-infected Gli36 target cells (Supplementary Fig. 3). When $KLRG1^-$ NK cells were used as effector cells, there was no difference in killing of OV-Q1- and OV-CDH1-infected GBM cells (Fig. 1b). However, when $KLRG1^+$ NK cells were used as effector cells, OV-CDH1-infected cells were killed significantly less than OV-Q1-infected cells (Fig. 1b). Notably, CD107a expression was

decreased when KLRG1$^+$ NK cells were incubated with OV-CDH1-infected cells as compared to OV-Q1-infected cells, but there was no difference between comparably co-cultured KLRG1$^-$ NK cells (Fig. 1c,d). We also evaluated NK cell secretion of IFN-γ, which can activate macrophages to phagocytose virus-infected cells[24], and found that KLRG1$^+$, but not KLRG1$^-$, NK cells secreted less IFN-γ when co-cultured with OV-CDH1-infected cells than with OV-Q1-infected cells (Fig. 1e).

Augment of cell-cell fusion and viral spread in OV-CDH1 infection

We next evaluated viral spread for OV-CDH1 and found that the GBM cell plaques formed by OV-CDH1 infection grew much faster and were much larger than those formed by OV-Q1 infection (Fig. 2a,b and Supplementary Videos 1,2). These data provide evidence for the enhanced viral spread of OV-CDH1 over parental oHSV, OV-Q1. We further studied the morphological changes within these plaques using distinctive staining for cell membrane and nuclei. While OV-Q1-infected cells were mononuclear with a distinct membrane structure for each cell, multiple nuclei gathered in the central area of OV-CDH1 plaques without obvious cell membrane structure separating them, indicating that the OV-CDH1-infected cells fused together as multinucleated syncytia (Fig. 2c). Membrane fusion has been previously reported to facilitate viral spread of wild-type HSV-1[25]. Using time-lapse plaque forming videos with labeled infected cells, we observed that GFP positive (OV-CDH1-infected) cells could directly fuse with the GFP negative (uninfected) cells, which subsequently became GFP positive (Supplementary Videos 3,4). In contrast, the OV-Q1-infected cells could not fuse with uninfected or infected neighboring cells. The time-lapse phase images showed an obvious cell membrane fusion process during OV-CDH1 spread (Supplementary Fig. 4,5,6). The caspase-3/7 staining showed that this cell fusion process was initiated with live cells, not dead cells (Supplementary Fig. 7). To better mimic the GBM microenvironment, semi-solid media (1.2% methylcellulose) were also used to repeat the plaque forming experiment. We observed that OV-CDH1 but not OV-Q1 plaques formed in the semi-solid media were larger than those formed in liquid media (Supplementary Fig. 8).

Increase of cell-to-cell infection of OV-CDH1 by cadherin interaction

To test whether ectopically expressed E-cad on OV-CDH1-infected cells contribute to enhanced viral spread, we used a neutralizing antibody that blocks the extracellular domain of E-cad[26]. As predicted, treatment with this antibody resulted in a significant reduction in plaque size after OV-CDH1, but not OV-Q1, infection (Supplementary Fig. 9). To further validate the specific role of the extracellular domain of E-cad in this process, we used OV-IL2RA-CDH1 to repeat the plaque forming experiment. Mutant E-cad did not induce cell-cell fusion or enhance viral spread (Fig. 3a). Moreover, there was no significant size difference observed between OV-IL2RA-CDH1 plaques and OV-Q1 plaques (Fig. 3b). Collectively, these results show that the extracellular domain of E-cad plays a direct role in triggering cell-cell fusion and enhancing viral spread of OV-CDH1.

While GBM cells do not express E-cad, they do express N-Cadherin (N-cad) that is encoded by the gene (*CDH2*), which can interact with E-cad to form heterodimers between neighboring cells[27]. We observed co-localization of human E-cad and human N-cad along

the interface between OV-CDH1-infected cells and uninfected cells (Fig. 3c; Supplementary Fig. 10). To determine whether the interaction between E-cad and N-cad is sufficient to induce cell fusion between OV-CDH1-infected cells and uninfected cells, we knocked down N-cad expression in Gli36 cells and performed a plaque forming assay (Fig. 3d). Knockdown of N-cad resulted in a significant decrease in plaque size following OV-CDH1 infection, but not following OV-Q1 infection (Fig. 3e,f), implying that the interaction between E-cad and N-cad may contribute to cell-cell fusion between OV-CDH1-infected and uninfected GBM cells, which leads to direct cell-to-cell infection.

Improvement of viral production and viral entry by OV-CDH1

We next evaluated the viral production capacity of OV-CDH1-infected cells and found that OV-CDH1 produced significantly more virus progeny than OV-Q1 following non-saturating infection *in vitro* (Fig. 4a,b). At 48 hpi, the viral production of OV-CDH1 in Gli36 and U251 cells was approximately 17-fold and 13-fold higher than OV-Q1, respectively (Fig. 4a,b). While we did not observe notable differences in viral production of OV-CDH1 and OV-Q1 at late time points (48, 72 and 96 hpi) following saturating infection, there was still 1.5 to 2-fold higher viral production of OV-CDH1 at 24 hpi (Fig. 4c,d). These results suggest that the enhancement of initial viral entry may also contribute to higher viral production of OV-CDH1.

We hypothesized that if E-cad was loaded on the viral membrane of OV-CDH1, it could expedite viral entry. Then, we confirmed the loading of E-cad on OV-CDH1 viral membrane (Supplementary Note 2; Supplementary Figure 11a,b,c). To test the viral entry kinetics of OV-CDH1 and OV-Q1, we infected Gli36 cells and cells were gently washed with PBS at varying timepoints following infection (5 to 360 min) to remove all unbound viral particles allowing the viruses that had entered cells to remain and replicate to form plaques. At 48 hpi, plaques were counted as representation of viral particles that entered the cells and viral entry vs. time curves were established to evaluate viral entry kinetics. Our data suggest that the viral entry speed of OV-CDH1 seemed to be faster than that of OV-Q1 (Fig. 4e), as only viruses that entered cells could form plaques and there was no viral production difference between OV-Q1 and OV-CDH1 at the late time points after saturating infection. A flow cytometry-based viral binding/entry kinetics assay validated the accelerated viral entry of OV-CDH1 (Supplementary Note 3**,** Supplementary Fig. 11d**)**.

Enhancement of GBM virotherapy *in vivo* by OV-CDH1

To evaluate the efficacy of OV-CDH1 on GBM therapy *in vivo*, we established xenograft GBM mouse models intracranially (i.c.) by injecting luciferase-expressing GBM30 cells or U87ΔEGFR cells into athymic nude mice[8]. 5 days after tumor implantation, animals were randomly assigned to undergo intratumoral injection with OV-CDH1, OV-Q1 or vehicle control. For the GBM30 model, mice underwent luciferase-based imaging to evaluate the progression of GBM at day 10 (Fig. 5a). OV-CDH1 was significantly more effective than OV-Q1 at reducing GBM tumor size *in vivo* (Fig. 5b,c). While OV-Q1 moderately slowed GBM progression as compared to vehicle control, all the imaged OV-CDH1-treated mice exhibited little to no detectable luciferase signal, suggesting substantial regression of tumor growth. Treatment with OV-CDH1 significantly prolonged the median survival time.

Moreover, all but one mouse from the OV-CDH1 group survived over 90 days without GBM symptoms; in contrast, median survival time of mice in the OV-Q1 group was 34 days (Fig. 5d). Staining of brain sections harvested 10 and 20 days after tumor implantation showed that tumor sizes of OV-Q1 treated mice were smaller than those of control mice, but still solid and compact (Fig. 5e). In OV-CDH1 treated mice, however, no solid tumors were observed (Fig. 5e). In the more aggressive U87ΔEGFR GBM model, OV-CDH1-treated mice still survived significantly longer than OV-Q1-treated mice (Fig. 5f).

We next sought to evaluate the efficacy of OV-CDH1 in an immunocompetent GBM mouse model. Immunocompetent GBM models to study oHSVs have been challenging to establish because human GBM cells cannot effectively develop tumors in immunocompetent backgrounds and because most murine GBM cells are resistant to oHSV infection[28–30] (Supplementary Fig. 12a). To overcome these problems, we used a murine GBM cell line (Gl261N4) engineered to express human nectin-1, a herpesvirus entry receptor[31]. Gl261N4 is thus susceptible to oHSV infection, although to a much lesser extent than human GBM cells (Supplementary Fig. 12a,b). Consistent with our previous data, Gl261N4 cells infected with OV-CDH1 showed obvious cell-cell fusion and significantly enhanced viral spread compared to Gl261N4 cells infected with OV-Q1 (Supplementary Fig. 12c,d). OV-CDH1-infected, but not OV-Q1-infected Gl261N4 cells, expressed E-Cad on the cell surface and co-localization of human E-cad and murine N-cad was observed along the interface between the OV-CDH1-infected cells and uninfected cells (Supplementary Fig. 13). By i.c. injecting Gl261N4 cells into immunocompetent wild-type C57BL/6 mice, we established a GBM immunocompetent mouse model and repeated the survival study. The treatment of these mice with OV-CDH1 significantly prolonged their median survival (42.5 days) when compared to identical mice treated with OV-Q1 (32 days) (Fig. 5g). Notably, without the extracellular domain of E-cad, OV-IL2RA-CDH1 did not show significant improvement in treating GBM when compared to OV-Q1 (Supplementary Fig. 14).

Improvement of viral spread and viral production *in vivo* by OV-CDH1

In order to further understand the effects of OV-CDH1 on the tumor microenvironment, we repeated these animal studies with a slightly altered timeline, wherein we implanted GBM30 cells and waited for 10 days, followed by a shorter oHSV treatment course of 3 days, to avoid complete tumor eradication (Fig. 6a). In the xenograft model, both OV-Q1 and OV-CDH1 recruited NK cells and macrophages to the brains, but brains treated with OV-CDH1 contained significantly more NK cells (Fig. 6b). There were no notable differences in macrophage or microglia recruitment between the two viruses (Fig. 6b). Consistent with our *in vitro* findings, OV-CDH1 specifically inhibited the cytotoxicity of $KLRG1^+$ but not $KLRG1^-$ NK cells *in vivo* (Fig. 6c,d). Similarly, histologic results showed that OV-CDH1 potentiated suppression of tumor development (Fig. 6e). Using immunohistochemistry staining with an anti-HSV antibody, we found enhanced viral spread and oncolysis in OV-CDH1-treated mice (Fig. 6f). Viral production assays further showed that OV-CDH1-treated brains had 7 times more viral DNA detected than those treated with OV-Q1 (Fig. 6g). In the immunocompetent GBM model, OV-CDH1 resulted in the recruitment of significantly more NK cells, macrophages and microglia as compared to treatment with OV-Q1 (Fig. 6h). The viral production of OV-CDH1 was also over 10 times higher than that of OV-Q1 (Fig. 6i),

which may explain why treatment with OV-CDH1 resulted in greater infiltration of NK cell, macrophage and microglia. We also evaluated frequencies of intracranial $CD4^+$ and $CD8^+$ T cells and found that these were significantly increased after both viral treatments, with no difference between the two (Fig. 6j,k). These *in vivo* studies not only confirmed OV-CDH1-mediated enhancement of viral spread and production, but also demonstrated an increased infiltration of NK cells that may due to the dramatically increased infectivity, while the cytotoxicity of $KRLG1^+$ NK cells among the infiltrated NK cells will be inhibited after OV-CDH1 infection.

Partial contribution of NK cell inhibition in OV-CDH1 virotherapy

To better determine the contributions of different immune cells to the improved therapeutic efficacy of OV-CDH1, we repeated the survival studies in the Gl261N4 model with or without depletion of NK cells, macrophages, $CD4^+$ or $CD8^+$ T cells. In particular, we sought to establish the relative importance of NK cell inhibition in mediating the effects seen with OV-CDH1 treatment. When NK cells were depleted, the survival of OV-Q1- and that of OV-CDH1-treated mice were both prolonged; however, there was a smaller but still significant difference in efficacy between OV-CDH1 and OV-Q1, suggesting that enhanced viral spread likely plays a larger role than NK cell inhibition in improving the efficacy of OV-CDH1 (Supplementary Fig. 15a). While macrophage depletion seemed to improve the efficacy of both OV-Q1 and OV-CDH1, the differences in median survival between OV-CDH1- and OV-Q1-treated mice were similar in both the presence and absence of macrophages (Supplementary Fig. 15b). This might be due to the fact that the $KLRG1^+$ NK cell subset is not a major population that produces IFN-γ (Fig. 1e), a cytokine that activates macrophages. Unlike NK cell or macrophage depletion, $CD8^+$ T cell depletion appeared to lower the therapeutic efficacy of both oHSVs (Supplementary Fig. 15c). In contrast, $CD4^+$ T cell depletion had no significant influence on survival (Supplementary Fig. 15d).

Safety profiling of OV-CDH1

OV-Q1 and OV-CDH1 both carry the HSV-1 TK gene, which renders the viruses sensitive to the antiviral acyclovir (Supplementary Fig. 16a), suggesting that viral replication can be stopped effectively as and when needed. To further evaluate the *in vivo* safety of OV-CDH1, BALB/c mice were intravenously (i.v.) or i.c. injected with wild-type HSV-1 (as a negative control for safety), OV-Q1 or OV-CDH1 at a high dose of 1×10^6 PFU. Mice injected with i.v. or i.c. wild-type HSV-1 died rapidly (5 days or less), while all mice treated with OV-Q1 and OV-CDH1 survived to the end of the 4-week study (Supplementary Fig. 16b). Bio-distribution of OV-CDH1 and OV-Q1 was evaluated using IHC staining for HSV-1 on sections of the heart, liver, spleen, lung, kidney and brain of mice treated for 2 days and both viruses exhibited similar patterns (Supplementary Table 1). Viral particles were primarily found in the liver and could not be detected in the heart, brain or spleen. We did not observe a discernible tropism change using OV-Q1 and OV-CDH1 infection of six different human primary cells (Supplementary Fig. 17**)**

Discussion

We demonstrate improvement of the therapeutic efficacy of oHSV by reducing its susceptibility to NK cell killing and enhancing its intratumoral spread through overexpression of E-cad. oHSV has two different modalities for spreading: viral particle diffusion to infect distant target cells and cell-to-cell infection. In the context of a solid tumor, many factors impair diffusion and therefore cell-to-cell infection may be the primary mechanism for viral spread. We show that OV-CDH1 forms larger plaques in semi-solid media than in liquid media via enhanced cell-to-cell infection mediated by E-cad. We hypothesize that overexpressing E-cad may strengthen the adherens junctions and shortens the distance between infected and uninfected cells and increase the regional concentration of nectin-1 to facilitate the viral spread.

We and others have demonstrated that NK cell depletion or pre-treatment with innate immune suppressive agents before virus administration results in significantly better outcomes in models of GBM, hepatocellular carcinoma and metastatic melanoma[7, 8, 10, 32–34]. Systemic inhibition of NK cells, however, inevitably causes reduced antitumor activity over the course of treatment. In this study, our goal was to specifically inhibit the antiviral activity of NK cells interacting with oHSV-infected tumor cells while maintaining the inherent anti-tumor activity of the remaining NK cells. While it was previously known that E-cad-expressing target cells inhibit the cytotoxicity of tumor-activated NK cells by binding to the receptor KLRG1[14–16], it was unclear whether virally activated NK cells could be inhibited by E-cad. Here we showed that even when NK cells have been activated by oHSV infection, E-cad can inhibit the antiviral cytotoxicity of $KLRG1^+$ NK cells by approximately half. This level of inhibition may provide more time for OV-CDH1 to complete viral reproduction and initiate secondary infection, leading to increased tumor killing and thus improving the efficacy of virotherapy. We note that the $KLRG1^-$ NK cells produce approximately 10-fold more IFN-γ than $KLRG1^+$ NK cells. Activated $CD56^{bright}$ NK cells are more potent IFN-γ producers, while $CD56^{dim}$ NK cells, which are largely $KLRG1^+$ (Supplementary Fig. 2a), are more cytolytic[35, 36]. This suggests that compared to inhibition of IFN-γ, inhibition of cytotoxicity by the E-cad-KLRG1 interaction plays a more important role in improving the efficacy of OV-CDH1. Consistent with this, our *in vivo* immune cell depletion data show that depletion of macrophage, which can be activated by IFN-γ, seemed not to specifically enhance the efficacy of OV-CDH1 but enhance the efficacy of both OV-Q1 and OV-CDH1.

As GBM is a heterogeneous cancer, we examined the efficacy of OV-CDH1 in three mouse models. OV-CDH1 showed significant improvement over parental OV-Q1 for the treatment of GBM both in the GBM30 and U87ΔEGFR xenograft models and in an engineered preclinical GL261 immune competent mouse model. In the GBM30 xenograft model, OV-CDH1 treatment resulted in a survival rate of nearly 100% in GBM-bearing mice and almost nearly eliminated the tumor tissue. Although the U87ΔEGFR GBM model is more aggressive due to the constitutively activated EGFR pathway, we still observed significant enhancement of OV therapy by OV-CDH1. Despite the low susceptibility of Gl261N4 cells to oHSV infection and limited performance of OV-CDH1 in immune competent GBM mice, OV-CDH1 treatment still significantly prolonged the survival of Gl261N4 GBM-bearing

mice when compared to OV-Q1 treatment. The differential efficacies of OV-CDH1 with these three GBM models may be due to intratumoral heterogeneity, which is an important and challenging component of human GBM. In addition to its apparent therapeutic efficacy in our experimental models, we demonstrate that OV-CDH1 possesses sensitivity to the antiviral acyclovir and it should be sensitive to other anti-herpetic agents[37]. This built-in safety feature should allow for virus clearance from a patient, if needed, following successful tumor treatment.

Currently, there are two main strategies for oHSV development. One is the attenuation strategy that is used by many oHSVs, including Imlygic, rQNestin34.5, or 34.5ENVE as well as our OV-CDH1[5, 38, 39]. In this approach, the viruses are modified with deletion or inactivation of some genes involved in viral replication to limit oHSV replication to proliferating tumor cells. However, this results in substantial restriction of viral spread and oncolysis. A second method involves retargeting oHSV to tumor cells by modifying the viral entry-related glycoproteins[40–42]. While these viruses maintain potent viral replication and production, the viral entry modifications can reduce viral infectivity[42]. In contrast to both of these approaches, E-cad significantly enhanced the viral spread of attenuated oHSV and improved its viral entry, directly contributing to the observed improvement in therapeutic efficacy. We have observed that enhanced viral spread of OV-CDH1 occurs not only in GBM but also in other solid cancers, including breast cancer (Supplementary Fig. 18). This suggests that E-cad can be added as a module to other HSV- and non-HSV-based oncolytic viruses to improve efficacy in treating cancers other than GBM.

Materials and Methods

Cells

Human GBM cell lines (Gli36, U251, U87 and U87ΔEGFR) and mouse GBM cell lines (Gl261 and Gl261N4) were maintained with DMEM media supplemented with 10% fetal bovine serum (FBS), penicillin (100 U/ml) and streptomycin (100 μg/ml). Gl261N4 cells were modified to express human nectin-1 to allow permissiveness to oHSV infection. GBM30 spheroid cells derived from a GBM patient and modified to express luciferase were named GBM30-FFL and used for *in vivo* imaging. The protocols for human specimen collection were approved by The Ohio State University Institutional Review Board. GBM30 and GBM30-FFL cells were maintained as tumor spheres with neurobasal media supplemented with 2% B27 (Gibco), human epidermal growth factor (20 ng/ml), and basic fibroblast growth factor (20 ng/ml) in low-attachment cell culture flasks. Monkey kidney epithelial-derived Vero cells maintained using the same media as the glioblastoma cell lines were used for viral propagation and plaque assay-based viral titration. To knock down N-cad expression in Gli36 cells, the cells were infected with lentivirus coding N-cad-shRNA (TRCN0000312701, Sigma). U87, Gli36, U251 and GBM30 cells were authenticated by the University of Arizona Genetics Core via STR profiling in January 2015 and Vero, Gl261 and Gl261N4 cells were not authenticated after receipt. All cell lines were obtained from the laboratory of E. Antonio Chiocca and routinely tested for absence of mycoplasma using MycoAlert™ PLUS Mycoplasma Detection Kit from Lonza (Walkersville, MD). Human primary cells including oral fibroblasts, pulmonary microvascular endothelial cells, hepatic

sinusoidal endothelial cells, pulmonary alveolar epithelial cells, neurons and neurons-midbrain were purchased from ScienCell and cultured following manufacturer's instructions.

Viruses

OV-CDH1 and OV-IL2RA-CDH1 were generated using the fHsvQuik-1 system as previously described[21]. Briefly, the full-length coding sequence of human *CDH1* gene was cloned and inserted into pT-oriSIE4/5 following the HSV pIE4/5 promoter to construct the pT-oriSIE4/5-CDH1. Then, pT-oriSIE4/5 and pT-oriSIE4/5-CDH1 were used to recombine with fHsvQuik-1 to engineer OV-Q1 and OV-CDH1, respectively. To generate OV-IL2RA-CDH1, the original E-cad extracellular domain was replaced with the extracellular domain of interleukin-2 receptor alpha chain (IL2RA). The cytoplasmic domain of E-cad remained intact[23]. Viruses were propagated and titrated using Vero cells. Virus titration was performed using plaque assays. Briefly, monolayer Vero cells were infected with gradient diluted viral solutions. Two hours after infection, the infection media were replaced with overlay media containing 1.2 % methylcellulose. GFP-positive plaques were counted with a Zeiss fluorescence microscope (AXIO observer.Z1) 2 days after infection for calculating the virus titer.

NK cell cytotoxicity assay

U87, Gli36, U251 and GBM30 cells were infected with OV-Q1, OV-CDH1 or OV-IL2RA-CDH1 at a MOI of 5. Eight hours after infection the infected cells were used as target cells. Effector cells were primary human NK cells isolated from leukopaks of health donors using an NK cell isolation kit (MACSxpress® Miltenyi Biotec, San Diego, CA) and an erythrocyte depletion kit (Miltenyi Biotec). Target cells were labeled with Chromium-51 (^{51}Cr) for 1 hour, and then co-cultured with bulk human primary NK cells or sorted KLRG1^{+} and KLRG1^{-} NK cells at different effector:target ratios at 37℃ for 4 hours. Release of ^{51}Cr was measured with a Beckman Liquid Scintillation Counter LS-6500 (Beckman Coulter, Fullerton, CA). Target cells incubated in complete media or 1% SDS media were used for spontaneous or maximal ^{51}Cr release control, respectively. The cell lysis percentages were calculated using the standard formula: 100 × (cpm experimental release – cpm spontaneous release) / (cpm maximal release – cpm spontaneous release). The assays were performed in at least three technical replicates with NK cells from different donors.

Plaque forming assay

To evaluate the viral spreading behavior in OV-CDH1, plaque forming assays were performed using monolayers of U251, Gli36 and Gl261N4 cells that were infected with OV-Q1, OV-CDH1 or OV-IL2RA-CDH1 at a MOI of 0.005. Two hours after infection, the infection media were replaced with fresh media or semi-solid media (1.2% methylcellulose). To investigate the role of E-cad in enhancing virus spread of OV-CDH1, the E-cad neutralizing antibody (clone DECMA-1) (100 ng/ml) or the gD neutralizing antibody (clone B007 LP2) (10 ng/ml) was included in the media. For distinctive staining, cell components, cell membrane and cell nuclei were labeled using Celltracker™ Deep Red, CellMask™ Deep Red and DAPI at 24 or 48 hpi, respectively. Apoptosis was assessed using CellEvent™ Caspase-3/7 Red staining at 48 hpi. For viral tropism assay and cell susceptibility test,

gradient (5 to 5,000) PFU of viruses were used for infection. The plaques in each group were imaged by using fluorescent microscopy at 24, 48 and 72 hpi or as needed. Videos of plaque formation were recorded with the Zeiss fluorescence microscope (AXIO observer. Z1) system from 24 to 72 hpi.

Viral production assay

For viral production assays, monolayers of U251 and Gli36 cells were infected with OV-Q1 or OV-CDH1 at a MOIs of 5 or 0.005. Two hours after infection, the infection media were replaced with fresh media. The supernatants from each group were then harvested at 24, 48, 72 and 96 hpi and virus titers were analyzed by plaque assays. The experiments were performed in three technical replicates.

Flow cytometry

To detect surface expression of human E-cad, OV-Q1- and OV-CDH1-infected glioblastoma cells were stained with an anti-hE-cad-APC antibody for 30 min in Ca^{2+} conditional staining buffer. To detect surface expression of human mutant E-cad (IL2RA/E-cad), an anti-CD25-APC antibody was used. For the CD107a degranulation assay, OV-infected or uninfected glioblastoma cells were co-cultured with NK cells at the ratio of 1:1 in the presence of an anti-CD107a-PE antibody at 8 phi. One hour later, GolgiStop™ (BD Biosciences) was added. After four hours' co-culture, the cells were harvested and stained with anti-CD56-APC-H7, anti-CD3-V450 and anti-KLRG1-APC antibodies for 30 minutes. This *in vitro* CD107a degranulation assay was repeated 3 times with independent donors. For *ex vivo* flow cytometric assessment of murine immune cells, mice were euthanized at the indicated time points. The mononuclear cells in the brain were extracted with Percoll and stained with anti-NKp46, anti-CD3, anti-CD115, anti-CD45, anti-CD11b, anti-CD4, anti-CD8, anti-KLRG1 and anti-CD107a antibodies for flow cytometric analysis of immune cells. The flow cytometric assessments of murine immune cells were performed with at least 3 independent animals. All flow cytometry data were collected using an LSR II cytometer (BD Biosciences). The flow cytometry gating strategy was described in Supplementary Figure 19.

Animal studies

Six- to eight-week-old female athymic nude mice and C57BL/6 mice were purchased from Jackson Laboratories (Bar Harbor, Maine). For the survival studies, the mice were anesthetized and stereotactically injected with 1×10^5 GBM cells (GBM30-FFL and U87ΔEGFR cells for nude mice and Gl261N4 cells for C57BL/6 mice) into the right frontal lobe of the brain (2 mm lateral and 1 mm anterior to bregma at a depth of 3 mm). The GBM cells (GBM30-FFL, U87ΔEGFR or Gl261N4) were allowed to grow for 5 days, and animals were subsequently randomly divided into groups that were injected intratumorally either with 2×10^5 PFU oHSV (OV-Q1, OV-CDH1 or OV-IL2RA-CDH1) in 3 μl of HBSS or with vehicle. Mice were subsequently monitored frequently for GBM disease progression and were sacrificed when they became moribund with neurologic impairments and obvious weight loss. For the *in vivo* mechanism study, nude mice and C57BL/6 mice were stereotactically injected with 1×10^5 GBM30-FFL or Gl261N4 cells, respectively, into the same site of brain mentioned above. The GBM cells were allowed to grow for 10 days and

the mice were subsequently intratumorally injected with 2×10^5 PFU oHSV (OV-Q1 or OV-CDH1) or vehicle. 3 or 7 days after oHSV injection, mice were sacrificed to harvest brain, followed by a flow cytometric assay, viral production assay and IHC assay. The survival studies involving depletions of immune cells were performed using the same Gl261N4 GBM model mentioned above. NK cells were depleted by i.p. injections of NK1.1 neutralizing antibody (clone PK136; 0.5 mg/mouse) twice, once on the day before virus injection and once two days after the virus injection. Macrophages were depleted by i.p. injections of clodronate liposomes (0.1 ml/mouse) using the same schedule as the NK cell depletion studies. $CD4^+$ and $CD8^+$ T cells were depleted by three-time i.p. injections of anti-CD4 (clone GK1.5; 0.5 mg/mouse) and anti-CD8 neutralizing antibodies (clone 53–6.7; 0.5 mg/mouse), respectively, once every three days beginning the day before virus injection. The corresponding isotypes and liposomes were used as controls. The depletion antibodies were all purchased from BioXcell. All animal work was approved by The Ohio State University Institutional Animal Care and Use Committee.

Immunoblot and quantitative PCR

Western blot was performed as previously described. Anti-hE-cad (DECMA-1 and 36/E-cadherin), anti-hN-cad (ab18203), anti-beta-actin (sc-1616), anti-HSV (ab20536) and the corresponding secondary antibodies were used. Viral copy numbers were measured by PCR with the primers and probes against gD (Forward: 5'-CAGCCCCGCTGGAACTACTAT-3'; Reverse: 5'-TCAGGAACCCCAGGTTATCCT-3'; Probe: VIC-5'-ACAGCTTCAGCGCCG-3'-TAMRA) to evaluate the *in vivo* viral production. Titrated purified OV-Q1 solution was used as standard control to calculate the viral copy number.

Immunohistochemistry and immunofluorescence assays

Mouse tissue isolated from OV-CDH1-, OV-Q1- or vehicle-treated GBM-bearing mice were placed in 10% neutral buffered formalin for a minimum of 72h. After paraffin embedding, 4 μm-thick sections were cut from the blocks. H&E staining and IHC staining with anti-HSV antibodies (Dako) were performed by the Comparative Pathology & Mouse Phenotyping Shared Resource, College of Veterinary Medicine, The Ohio State University. The stained slides were mounted and viewed with a Zeiss microscope (AXIO observer. Z1).

Immunofluorescence studies were performed with OV-Q1- and OV-CDH1-infected human (U251) and mouse (Gl261N4) GBM cells at 48 hpi. Antibodies recognizing hE-cad (clone HECD-1) and N-cad (clone D4R1H, recognizing both human and mouse N-cad) were used to stain the cells and determine the location of human E-cad, human N-cad and mouse N-cad.

IFN-γ release assay

Human primary NK cells were incubated with target cells at the ratio of 1:1 in 96-well V bottom plates for 18 h. Cell-free supernatants were harvested and assayed for IFN-γ secretion by enzyme-linked immunosorbent assay (ELISA) using a kit from R&D Systems (Minneapolis, MN) in accordance with the manufacturer's protocol. Data depicted in figures represent mean values of triplicate wells from one of three representative experiments with similar results. The assay was repeated in 3 times with NK cells form different donors.

Viral entry kinetics assay

A modified plaque forming assay was performed for measuring viral entry kinetics of OV-CDH1. Briefly, 30,000 Gli36 cells per well were seeded on 96-well plates. The cells were grown overnight, followed by replacing the culture media with fresh media containing 150 PFU of OV-Q1 or OV-CDH1. Infection media were aspirated at 5, 10, 20, 40, 60, 90,120, 180, 240, 300 or 360 min post infection. Following the aspiration of infection media, cells were washed twice with PBS to remove un-entered/unbound viruses and then the overlay medium with 1.2% methylcellulose was added to cover the cells. This was to keep viruses that had entered cells but to remove un-entered/unbound virus, resulting in different groups with different viral incubation time. 48 hours after infection, the number of plaques (GFP positive) were counted with a fluorescence microscope. Data from the OV-Q1 and OV-CDH1 groups were normalized to the respective maximum number of plaques from 360 min incubation. Viral entry kinetics curves were established by relating the relative plaque numbers to viral incubation time for evaluating the viral entry speeds of OV-Q1 and OV-CDH1.

Statistics

For continuous endpoints that are normally distributed or normally distributed after data transformation (e.g., NK cell cytotoxicity, ^{51}Cr release, IFN-γ levels, viral production, etc), Student's *t* test was utilized to compare two independent conditions and one-way ANOVA model was utilized to compare three or more conditions. For data with repeated measures from the same donor (e.g., CD107a expression), linear mixed model was utilized to account for the variance-covariance structure due to repeated measures. *P* values were adjusted for multiple comparisons by Holm's procedure. Survival data were estimated by the Kaplan-Meier method and compared by the two-sided log rank test. Nonlinear models were fitted for each treatment group over time by Generalized Additive Model (R package "mgcv") and F test was used to compare the residual sum of squares. All tests were two-sided. Data are presented as mean ± SD. Error bars indicate SD. A *P* value of 0.05 or less was considered statistically significant.

Supplementary Material

Refer to Web version on PubMed Central for supplementary material.

Acknowledgements

This work was supported by grants from the NIH (NS106170, AI129582, J.Y.; CA185301, CA068458, CA210087, M.A.C.; and CA163205, E.A.C.; M.A.C.), the Leukemia & Lymphoma Society (6503–17, 1364–19, JY), the American Cancer Society Scholar Award (RSG-14–243-01-LIB, J.Y.), the National Key R&D Program (2018YFC1313400, Y.P.), and the Gabrielle's Angel Cancer Research Foundation (#87, J.Y.). The authors thank Ahmet Yilmaz, Betina McNeil and Victoria Sellers for critical reading.

References

1. Markert JM et al. Phase Ib trial of mutant herpes simplex virus G207 inoculated pre-and post-tumor resection for recurrent GBM. Mol. Ther. 17, 199–207 (2009). [PubMed: 18957964]

2. Kaufman HL & Bines SD OPTIM trial: a Phase III trial of an oncolytic herpes virus encoding GM-CSF for unresectable stage III or IV melanoma. Future Oncol. 6, 941–949 (2010). [PubMed: 20528232]

3. Hu JC et al. A phase I study of OncoVEXGM-CSF, a second-generation oncolytic herpes simplex virus expressing granulocyte macrophage colony-stimulating factor. Clin. Cancer Res. 12, 6737–6747, (2006). [PubMed: 17121894]

4. Nakamori M et al. Effective therapy of metastatic ovarian cancer with an oncolytic herpes simplex virus incorporating two membrane fusion mechanisms. Clin. Cancer Res. 9, 2727–2733 (2003). [PubMed: 12855653]

5. Pol J, Kroemer G & Galluzzi L First oncolytic virus approved for melanoma immunotherapy. Oncoimmunology 5, e1115641 (2016). [PubMed: 26942095]

6. Ikeda K et al. Oncolytic virus therapy of multiple tumors in the brain requires suppression of innate and elicited antiviral responses. Nat. Med. 5, 881–887, (1999). [PubMed: 10426310]

7. Alvarez-Breckenridge CA et al. NK cells impede glioblastoma virotherapy through NKp30 and NKp46 natural cytotoxicity receptors. Nat. Med. 18, 1827–1834 (2012). [PubMed: 23178246]

8. Han J et al. TGFbeta Treatment Enhances Glioblastoma Virotherapy by Inhibiting the Innate Immune Response. Cancer Res. 75, 5273–5282 (2015). [PubMed: 26631269]

9. Kolodkin-Gal D et al. Herpes simplex virus type 1 preferentially targets human colon carcinoma: role of extracellular matrix. J. Virol. 82, 999–1010 (2008). [PubMed: 17977977]

10. Fulci G et al. Cyclophosphamide enhances glioma virotherapy by inhibiting innate immune responses. Proc. Natl. Acad. Sci. USA a 103, 12873–12878 (2006).

11. Ayala-Breton C, Suksanpaisan L, Mader EK, Russell SJ & Peng KW Amalgamating oncolytic viruses to enhance their safety, consolidate their killing mechanisms, and accelerate their spread. Mol. Ther. 21, 1930–1937 (2013). [PubMed: 23842448]

12. Guedan S et al. Hyaluronidase expression by an oncolytic adenovirus enhances its intratumoral spread and suppresses tumor growth. Mol. Ther. 18, 1275–1283 (2010). [PubMed: 20442708]

13. Simpson GR et al. Combination of a fusogenic glycoprotein, prodrug activation, and oncolytic herpes simplex virus for enhanced local tumor control. Cancer Res. 66, 4835–4842 (2006). [PubMed: 16651439]

14. Ito M et al. Killer cell lectin-like receptor G1 binds three members of the classical cadherin family to inhibit NK cell cytotoxicity. J. Exp. Med. 203, 289–295 (2006). [PubMed: 16461340]

15. Li Y et al. Structure of natural killer cell receptor KLRG1 bound to E-cadherin reveals basis for MHC-independent missing self recognition. Immunity 31, 35–46 (2009). [PubMed: 19604491]

16. Schwartzkopff S et al. Tumor-associated E-cadherin mutations affect binding to the killer cell lectin-like receptor G1 in humans. J. Immunol. 179, 1022–1029 (2007). [PubMed: 17617594]

17. Drees F, Pokutta S, Yamada S, Nelson WJ & Weis WI Alpha-catenin is a molecular switch that binds E-cadherin-beta-catenin and regulates actin-filament assembly. Cell 123, 903–915 (2005). [PubMed: 16325583]

18. Tachibana K et al. Two cell adhesion molecules, nectin and cadherin, interact through their cytoplasmic domain-associated proteins. J. Cell Biol. 150, 1161–1176 (2000). [PubMed: 10974003]

19. Geraghty RJ, Krummenacher C, Cohen GH, Eisenberg RJ & Spear PG Entry of alphaherpesviruses mediated by poliovirus receptor-related protein 1 and poliovirus receptor. Science 280, 1618–1620 (1998). [PubMed: 9616127]

20. Stupp R et al. Effects of radiotherapy with concomitant and adjuvant temozolomide versus radiotherapy alone on survival in glioblastoma in a randomised phase III study: 5-year analysis of the EORTC-NCIC trial. Lancet. Oncol. 10, 459–466 (2009). [PubMed: 19269895]

21. Terada K, Wakimoto H, Tyminski E, Chiocca EA & Saeki Y Development of a rapid method to generate multiple oncolytic HSV vectors and their in vivo evaluation using syngeneic mouse tumor models. Gene Ther. 13, 705–714 (2006). [PubMed: 16421599]

22. Mineta T, Rabkin SD, Yazaki T, Hunter WD & Martuza RL Attenuated multi-mutated herpes simplex virus-1 for the treatment of malignant gliomas. Nat. Med. 1, 938–943 (1995). [PubMed: 7585221]

23. Gottardi CJ, Wong E & Gumbiner BM E-cadherin suppresses cellular transformation by inhibiting beta-catenin signaling in an adhesion-independent manner. J. Cell Biol. 153, 1049–1060 (2001). [PubMed: 11381089]
24. Bolyard C et al. BAI1 Orchestrates Macrophage Inflammatory Response to HSV Infection-Implications for Oncolytic Viral Therapy. Clin. Cancer Res. 23, 1809–1819 (2017). [PubMed: 27852701]
25. Kim IJ, Chouljenko VN, Walker JD & Kousoulas KG Herpes simplex virus 1 glycoprotein M and the membrane-associated protein UL11 are required for virus-induced cell fusion and efficient virus entry. J. Virol. 87, 8029–8037 (2013). [PubMed: 23678175]
26. Qian X, Karpova T, Sheppard AM, McNally J & Lowy DR E-cadherin-mediated adhesion inhibits ligand-dependent activation of diverse receptor tyrosine kinases. EMBO J. 23, 1739–1748 (2004). [PubMed: 15057284]
27. Labernadie A et al. A mechanically active heterotypic E-cadherin/N-cadherin adhesion enables fibroblasts to drive cancer cell invasion. Nat. Cell Biol. 19, 224–237 (2017). [PubMed: 28218910]
28. Halford WP, Balliet JW & Gebhardt BM Re-evaluating natural resistance to herpes simplex virus type 1. J. Virol. 78, 10086–10095 (2004). [PubMed: 15331741]
29. Cheema TA et al. Multifaceted oncolytic virus therapy for glioblastoma in an immunocompetent cancer stem cell model. Proc. Natl. Acad. Sci. USA 110, 12006–12011 (2013). [PubMed: 23754388]
30. Lopez C Genetics of natural resistance to herpesvirus infections in mice. Nature 258, 152–153 (1975). [PubMed: 171586]
31. Nakashima H et al. Toxicity and Efficacy of a Novel GADD34-expressing Oncolytic HSV-1 for the Treatment of Experimental Glioblastoma. Clin. Cancer Res. 24, 2574–2584 (2018). [PubMed: 29511029]
32. Bridle BW et al. HDAC inhibition suppresses primary immune responses, enhances secondary immune responses, and abrogates autoimmunity during tumor immunotherapy. Mol. Ther. 21, 887–894 (2013). [PubMed: 23295947]
33. MacTavish H et al. Enhancement of vaccinia virus based oncolysis with histone deacetylase inhibitors. PloS One 5, e14462 (2010). [PubMed: 21283510]
34. Altomonte J et al. Enhanced oncolytic potency of vesicular stomatitis virus through vector-mediated inhibition of NK and NKT cells. Cancer Gene Ther. 16, 266–278 (2009). [PubMed: 18846115]
35. Fehniger TA et al. CD56bright natural killer cells are present in human lymph nodes and are activated by T cell-derived IL-2: a potential new link between adaptive and innate immunity. Blood 101, 3052–3057 (2003). [PubMed: 12480696]
36. Nagler A, Lanier LL, Cwirla S & Phillips JH Comparative studies of human FcRIII-positive and negative natural killer cells. J Immunol. 143, 3183–3191 (1989). [PubMed: 2530273]
37. Markert JM, Malick A, Coen DM & Martuza RL Reduction and elimination of encephalitis in an experimental glioma therapy model with attenuated herpes simplex mutants that retain susceptibility to acyclovir. Neurosurgery 32, 597–603 (1993). [PubMed: 8386343]
38. Kambara H, Okano H, Chiocca EA & Saeki Y An oncolytic HSV-1 mutant expressing ICP34.5 under control of a nestin promoter increases survival of animals even when symptomatic from a brain tumor. Cancer Res. 65, 2832–2839 (2005). [PubMed: 15805284]
39. Bolyard C et al. Doxorubicin synergizes with 34.5ENVE to enhance antitumor efficacy against metastatic ovarian cancer. Clin. Cancer Res. 20, 6479–6494 (2014). [PubMed: 25294909]
40. Menotti L et al. Inhibition of human tumor growth in mice by an oncolytic herpes simplex virus designed to target solely HER-2-positive cells. Proc. Natl. Acad. Sci. USA 106, 9039–9044 (2009). [PubMed: 19458262]
41. Gatta V, Petrovic B & Campadelli-Fiume G The Engineering of a Novel Ligand in gH Confers to HSV an Expanded Tropism Independent of gD Activation by Its Receptors. PLoS pathog. 11, e1004907 (2015). [PubMed: 25996983]
42. Uchida H et al. Effective treatment of an orthotopic xenograft model of human glioblastoma using an EGFR-retargeted oncolytic herpes simplex virus. Mol. Ther. 21, 561–569 (2013). [PubMed: 23070115]

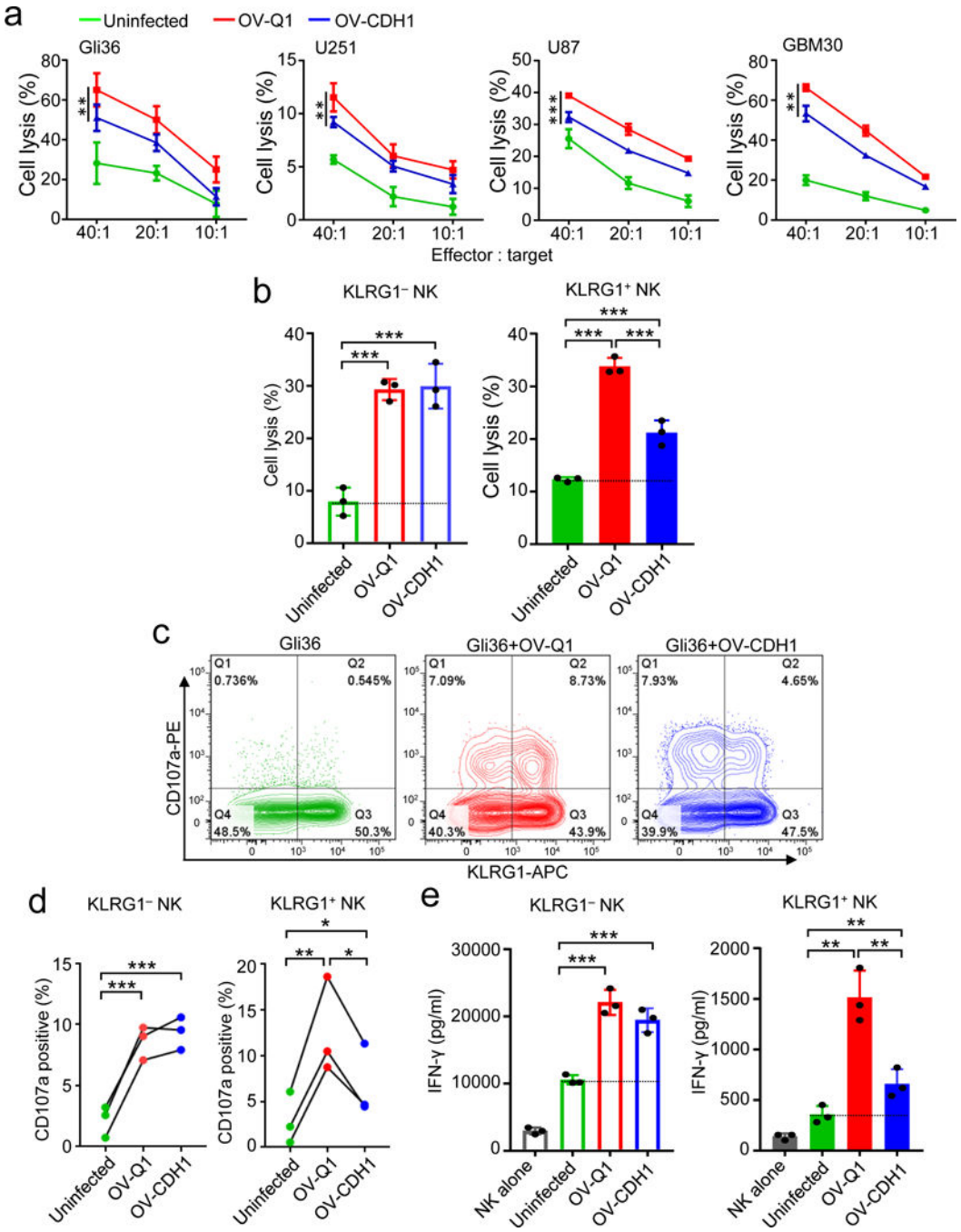

Figure 1. OV-CDH1 infection reduces the cytotoxicity of human NK cells against OV-infected GBM cells.

(a) Cytotoxicity of primary NK cells against uninfected, OV-Q1- or OV-CDH1-infected GBM cell lines at effector:target ratios of 40:1, 20:1 and 10:1. Data are presented as mean ± SD. OV-Q1 vs. OV-CDH1 $^{**}P < 0.01$; $^{***}P < 0.001$ by linear mixed model ($n = 3$ technical replicates). **(b)** The cytotoxicity of FACS-sorted KLRG1^{+} and KLRG1^{-} NK cell subsets against uninfected, OV-Q1- or OV-CDH1-infected Gli36 target cells at effector:target ratio of 30:1. Data are presented as mean ± SD. $^{***}P < 0.001$, $n = 3$ technical replicates by one-

way ANOVA with Holm's multiple comparisons test. (**c**) Degranulation of KLRG1$^+$ and KLRG1$^-$ NK cells co-cultured with uninfected, OV-Q1- or OV-CDH1-infected Gli36 cells at a ratio of 1:1 as measured by CD107a expression. (**d**) Statistical analysis of (**c**). For KLRG1$^+$ NK cells, uninfected vs. OV-Q1 $^{**}P = 0.003$; uninfected vs. OV-CDH1 $^{*}P = 0.027$; OV-Q1 vs. OV-Q1 $^{*}P = 0.013$. For KLRG1$^-$ NK cells, uninfected vs. OV-Q1 $^{***}P < 0.001$; uninfected vs. OV-CDH1 $^{***}P < 0.001$. *P* values were generated by one-way ANOVA with Holm's multiple comparisons test ($n = 3$ donors). (**e**) IFN-γ secretion from KLRG1$^+$ and KLRG1$^-$ human primary NK cells co-cultured with uninfected, OV-Q1- or OV-CDH1-infected Gli36 cells at a ratio of 1:1 as measured by ELISA. Data are presented as mean ± SD. For KLRG1$^+$ NK cells, uninfected vs. OV-Q1 $^{**}P = 0.008$; uninfected vs. OV-CDH1 $^{**}P = 0.003$; OV-Q1 vs. OV-Q1 $^{**}P = 0.002$. For KLRG1$^-$ NK cells, uninfected vs. OV-Q1 $^{***}P < 0.001$; uninfected vs. OV-CDH1 $^{***}P < 0.001$. *P* values were generated by one-way ANOVA with Holm's multiple comparisons test ($n = 3$ technical replicates). Experiments in a, b, e were repeated 3 times with NK cells isolated from different donors with similar results.

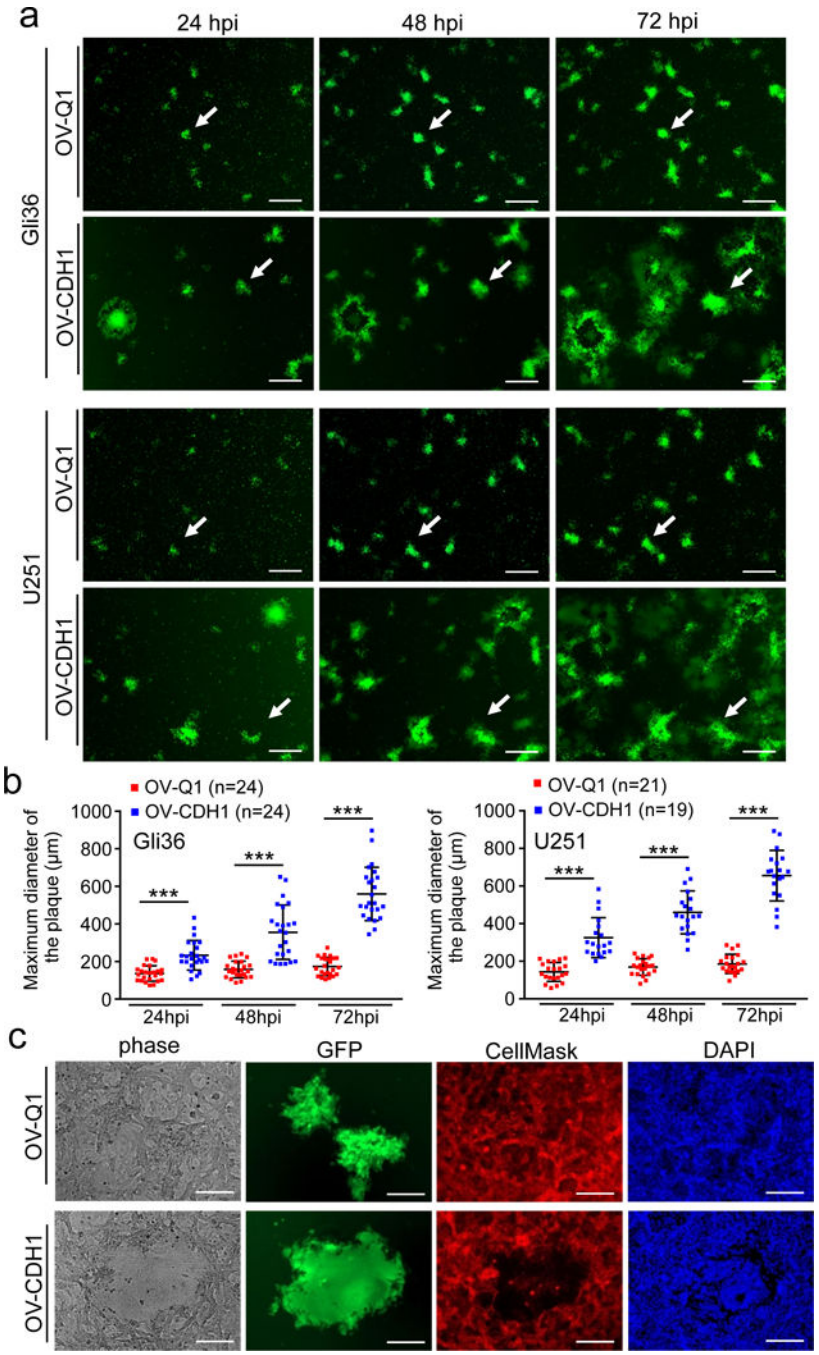

Figure 2. Cell-cell fusion facilitates viral spread of OV-CDH1.

(**a**) Monolayers of Gli36 and U251 cells were infected with OV-Q1 or OV-CDH1 at a MOI of 0.005. Cells were imaged with a fluorescence microscope at 24, 48 and 72 hpi. Each row shows same depiction of the cells at different time points. The white arrows in each row point out the same plaque from frame to frame to show the plaque forming process. Scale bar, 500 μm. (**b**) Statistical analysis of (**a**). Three random depictions from each group were selected for measuring plaque sizes. Data are presented as mean ± SD, ***$P < 0.001$ by unpaired two-tailed *t*-test. Sample sizes are indicated in the figures. (**c**) Monolayer Gli36

cells were infected with OV-Q1 or OV-CDH1 at a MOI of 0.005. Cells were stained with membrane and nuclear dye at 48 hpi and imaged with a fluorescence microscope. Green fluorescence (GFP) indicates the viral-infected cells; Red fluorescence indicates the cell membrane stained with CellMask; Blue fluorescence indicates cell nuclei stained with DAPI. Scale bar, 150 μm. The experiments in (**a**-**c**) were repeated 5 times independently with similar results.

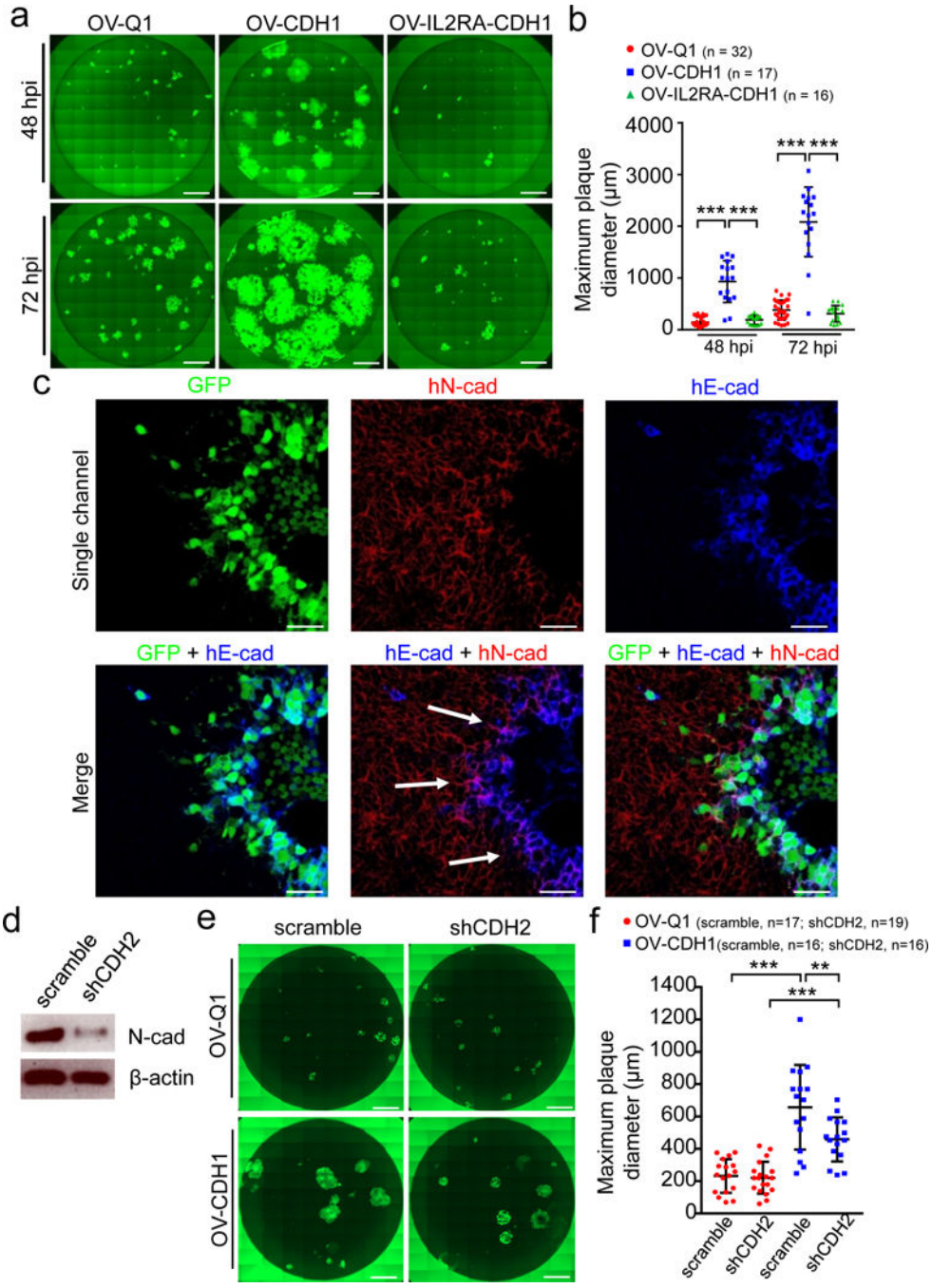

Figure 3. Cadherin interaction facilitates cell-to-cell infection by OV-CDH1.

(**a**) Monolayer U251 cells in 96-well plates were infected with OV-Q1, OV-CDH1 and OV-IL2RA-CDH1. Infection media were replaced with semi-solid media containing 1.2 % methylcellulose at 2 hpi. Cells were then imaged at 48 and 72 hpi with a fluorescence microscope. Scale bar, 1,000 μm. (**b**) Quantification of plaque diameter in (a). Data are presented as mean ± SD, ***$P < 0.001$ by one-way ANOVA with Holm's multiple comparisons test. Sample sizes are indicated in the figures. (**c**) U251 cells were infected with OV-CDH1. At 48 hpi, cells were blocked and incubated with anti-E-cad and anti-N-cad

antibodies, and followed by fluorescence secondary antibody staining. Cells were then observed under a confocal microscope. Scale bar, 50 μm. The experiments in (**a**-**c**) were repeated 5 times with similar results. (**d**) The expression of N-cad in Gli36 cells was knocked down with shRNA (shCDH2). The protein levels of N-cad were measured by immunoblotting. (**e**) Monolayer Gli36 cells with or without N-cad knock-down were seeded in 96-well plates and infected with OV-Q1 or OV-CDH1 at a MOI of 0.005. Cells were imaged using a fluorescent microscope at 48 hpi. Scale bar, 1,000 μm. (**f**) Quantification of plaque diameter in (**e**). Data are presented as mean ± SD. Scramble-OV-Q1 vs. scramble-OV-CDH1 ***$P < 0.001$; shCDH2-OV-Q1 vs. shCDH2-OV-CDH1 ***$P < 0.001$; scramble-OV-CDH1 vs. shCDH2-OV-CDH1 **$P = 0.002$. *P* values were generated by one-way ANOVA with Holm's multiple comparisons test. Sample sizes are indicated in the figures. The experiments in (**d**-**f**) were repeated 3 times with similar results. All images in (**a**) and (**e**) are stitched images.

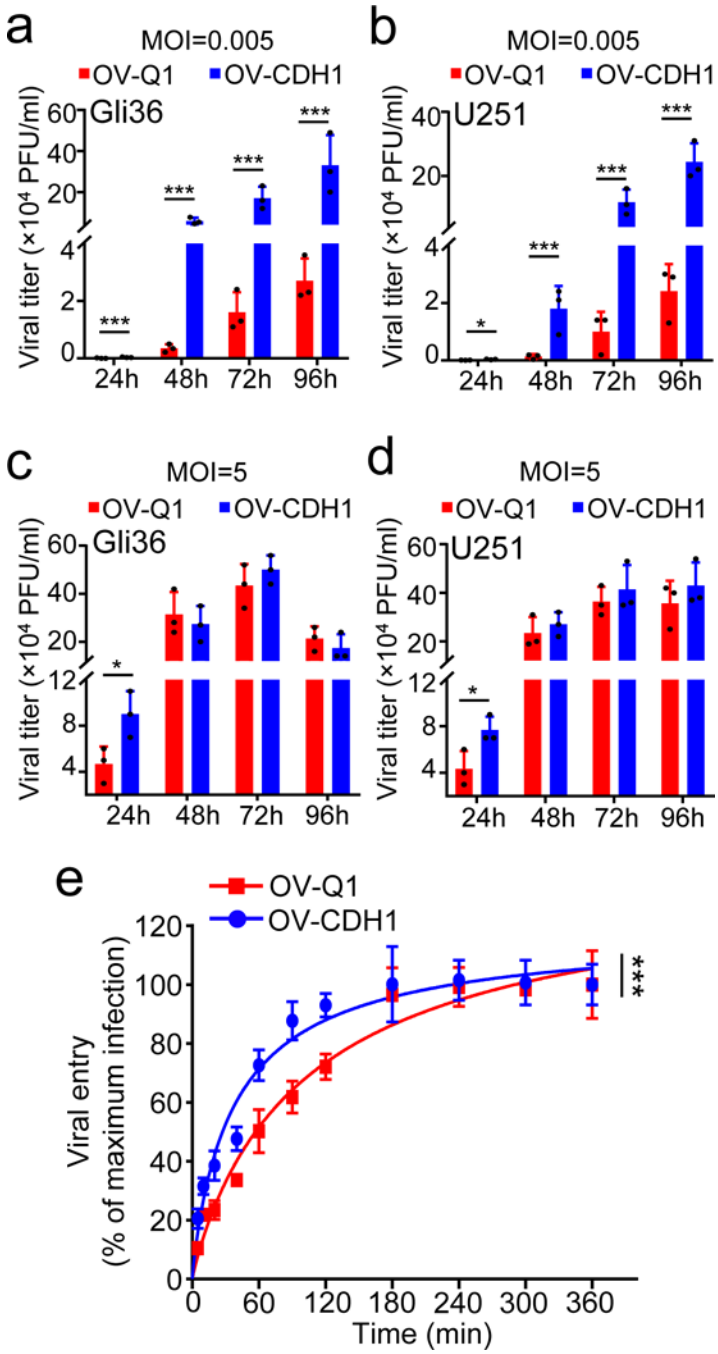

Figure 4. E-cad may accelerate viral entry and virus production.

(**a, b**) Monolayer Gli36 or U251 cells were infected with OV-Q1 or OV-CDH1 at a MOI of 0.005. At 2 hpi, infection media were replaced by fresh media. At 24, 48, 72 and 96 hpi, the supernatant viral titers were measured by plaque assay. (**c, d**) Gli36 or U251 cells were infected with OV-Q1 or OV-CDH1 at a MOI of 5. At 2 hpi, infection media were replaced with fresh media. At 24, 48, 72 and 96 hpi, the supernatant viral titers were measured by plaque assay. Data are presented as mean ± SD. For Gli36 cells infected with viruses at a MOI of 0.005, OV-Q1 vs. OV-CDH1 at 24 hpi ***$P < 0.001$; at 48 hpi ***$P < 0.001$; at 72

hpi ***$P < 0.001$; at 96 hpi ***$P < 0.001$. For U251 cells infected with viruses at a MOI of 0.005, OV-Q1 vs. OV-CDH1 at 24 hpi *$P = 0.035$; at 48 hpi ***$P < 0.001$; at 72 hpi ***$P < 0.001$; at 96 hpi ***$P < 0.001$. For Gli36 cells infected with viruses at a MOI of 5, OV-Q1 vs. OV-CDH1 at 24 hpi *$P = 0.024$. For U251 cells infected with viruses at a MOI of 5, OV-Q1 vs. OV-CDH1 at 24 hpi *$P = 0.026$. All P values in were generated by unpaired two-tailed t-test after log2 data transformation ($n = 3$ technical replicates). The experiments in (**a-d**) were repeated 4 times with similar results. (**e**) Viral entry kinetics assay of OV-CDH1 and OV-Q1. Monolayer Gli36 cells were infected with 150 PFU of OV-CDH1 or OV-Q1. At 5, 10, 20, 40, 60, 90, 120, 180, 240, 300 and 360 min after infection, infection media were removed and cells were gently washed twice with PBS before semi-solid media were replaced. At 48 hpi, the plaque numbers were counted. Viral entry vs. time curves were established to evaluate the viral entry kinetics of OV-CDH1. The overall group difference in the viral entry kinetics between OV-Q1 and OV-CDH1 was evaluated by linear model on log2 transformed data over time (***$P < 0.001$, $n = 3$ technical replicates). The experiment in (**e**) was repeated 3 times with similar results.

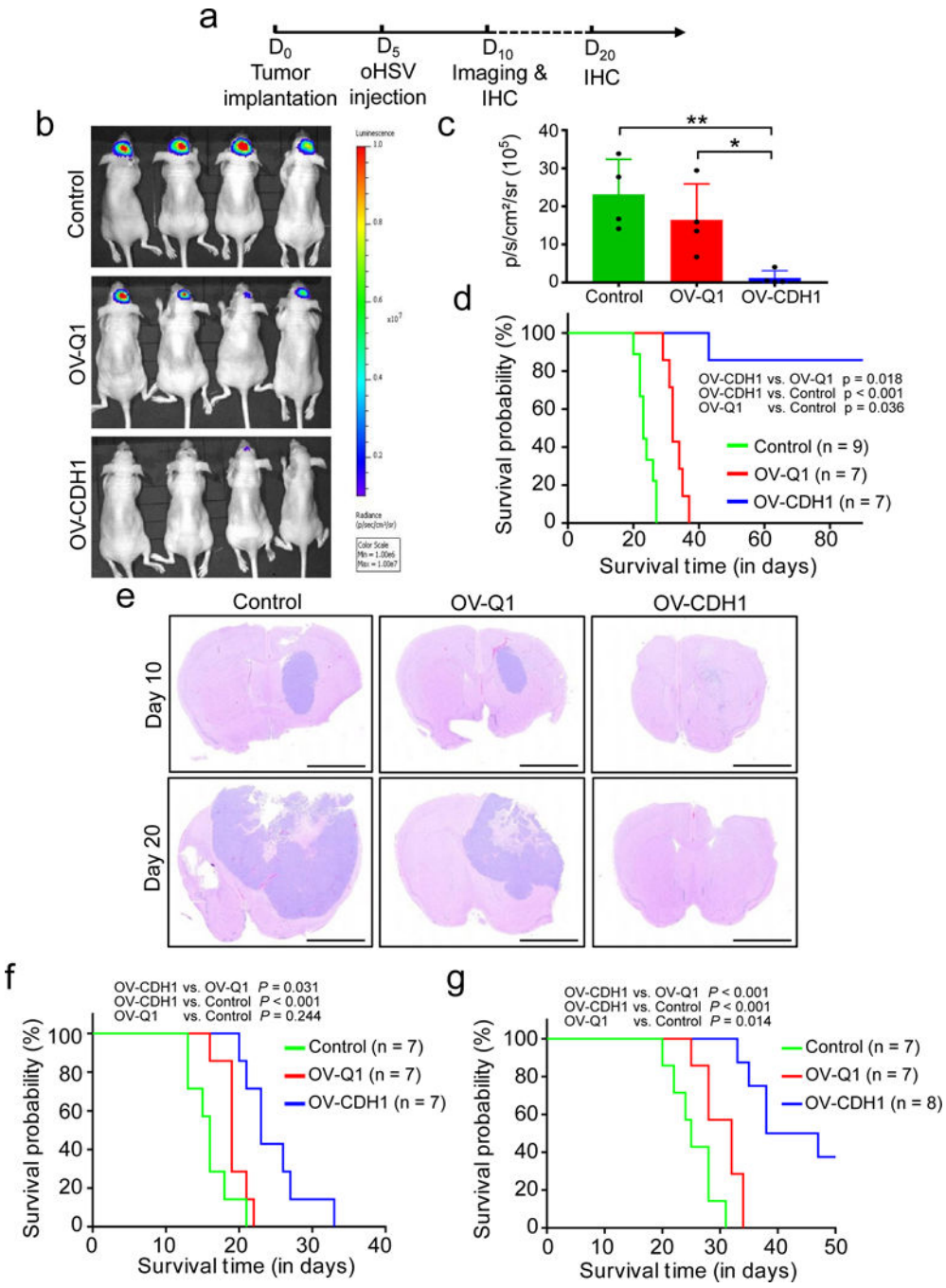

Figure 5. OV-CDH1 improves the efficacy of GBM virotherapy *in vivo*.

(**a**) Experimental timeline for *in vivo* studies. Xenograft and immunocompetent GBM mouse models were established by intracranially injecting 1×10^5 GBM30 or Gl261N4 cells to athymic nude mice or C57BL/6 mice, respectively. 5 days later, mice were intratumorally injected with 2×10^5 PFU of OV-CDH1, OV-Q1, or vehicle. (**b**) Luciferase imaging of GBM30 brain tumors 10 days after implantation. (**c**) Quantification of luciferase expression in (**b**). Data in are presented as the mean ± SD. control vs. OV-CDH1 $^{**}P = 0.009$; OV-Q1 vs. OV-CDH1 $^{*}P = 0.024$ ($n = 4$ animals). *P* values were generated by one-way ANOVA

with Holm's multiple comparisons test. (**d**) Survival of GBM30 tumor-bearing mice treated with vehicle control, OV-Q1, or OV-CDH1 as indicated in (**a**). (**e**) H&E stained coronal sections of GBM30 tumor-bearing mouse brains treated as indicated, 10 (top) or 20 (bottom) days after tumor cell implantation. Representative images of each group ($n = 3$ animals) are presented. Scale bar, 2,000 μm. (**f**) Survival curves of U87△EGFR tumor-bearing nude mice treated with vehicle control, OV-Q1 or OV-CDH1 as indicated in (a). (**g**) Survival of Gl261N4 tumor-bearing C57BL/6 immunocompetent mice treated with vehicle control, OV-Q1, or OV-CDH1 as indicated in (**a**). Two-sided log rank test was used to compare animal survival and *P* values and sample sizes are indicated in the corresponding figures (**d,f,g**).

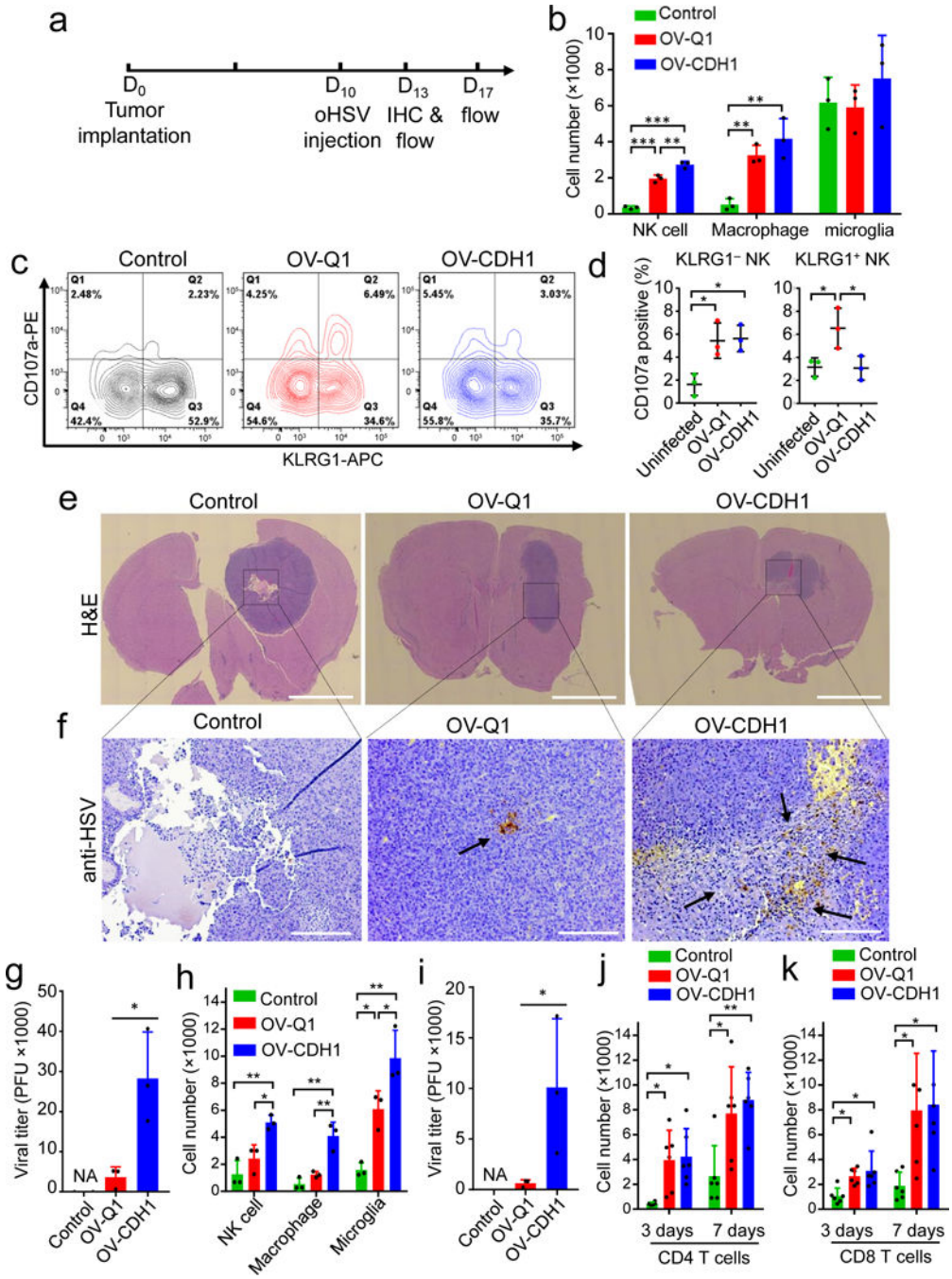

Figure 6. OV-CDH1 treatment leads to increased intracranial NK cell infiltration, enhanced viral spread, viral production and oncolysis.

(**a**) Experimental timeline for *in vivo* studies in **b**-**k**. (**b**) Number of NK cells ($CD3^{-}NKp46^{+}$), macrophages ($CD115^{+}CD45^{high}CD11b^{+}$), and microglia ($CD115^{+}CD45^{low}CD11b^{+}$) isolated from the brains of GBM30 tumor-bearing mice. Data are presented as mean ± SD. The *P* values of control vs. OV-Q1, control vs. OV-CDH1, and OV-Q1 vs. OV-CDH1 in NK cell and macrophage infiltrations are ***$P < 0.001$, ***$P < 0.001$, **$P = 0.001$ and **$P = 0.008$, **$P = 0.003$, $P = 0.182$, respectively, by one-way

ANOVA with Holm's multiple comparisons test ($n = 3$ animals). (**c**) CD107a and KLRG1 expression in NK cells isolated from mouse brains 3 days after virus injection. Representative flow cytometric plots of each group ($n = 3$ animals). (**d**) Quantification of CD107a expression, presented as mean ± SD, in $KLRG1^+$ and $KLRG1^-$ NK cell fractions in (**c**). For $KRLG1^+$ NK cells, uninfected vs. OV-Q1 $*P = 0.045$, OV-Q1 vs. OV-CDH1 $*P = 0.045$ and for $KLRG1^-$ NK cell, uninfected vs. OV-Q1 $*P = 0.022$, uninfected vs. OV-CDH1 $*P = 0.022$, by one-way ANOVA with Holm's multiple comparisons test ($n = 3$ animals). (**e, f**) Low magnification H&E stained (scale bar, 2000 μm, **e**) and anti-HSV stained (scale bar, 250 μm, **f**) coronal brain sections of GBM30 tumor-bearing mice. Brown pointed by arrows, HSV-1. Representative images of each group ($n = 3$ animals) are presented. (**g**) Virus titers in the brains of the OV-treated nude mice 3 days after OV injection. Bar graphs display mean ± SD and $*P = 0.035$ by unpaired two-tailed *t*-test after log2 data transformation ($n = 3$ animals). (**h**) The intracranial infiltrations of NK cells ($CD3^-NKp46^+$), macrophages ($CD115^+CD45^{high}CD11b^+$) and microglia ($CD115^+CD45^{low}CD11b^+$) in Gl261N4-bearing mice measured by flow cytometry 3 days after virus injection. Bar graphs display mean ± SD. The *P* values of control vs. OV-Q1, control vs. OV-CDH1, and OV-Q1 vs. OV-CDH1 in NK cell, macrophage and microglia infiltrations are $P = 0.154$, $**P = 0.005$, $*P = 0.020$ and $P = 0.237$, $**P = 0.002$, $**P = 0.003$ and $*P = 0.018$, $**P = 0.001$, $*P = 0.019$, respectively, by one-way ANOVA with Holm's multiple comparisons test ($n = 3$ animals). (**i**) Virus titers in the brains of the OV-treated C57BL/6 mice 3 days after virus injection. Bar graphs display mean ± SD and $*P = 0.012$ by unpaired two-tailed *t*-test after log2 data transformation ($n = 3$ animals). (**j, k**) The intracranial infiltrations of $CD4^+$ T cells ($CD3^+CD4^+$) (**j**) and $CD8^+$ T cells ($CD3^+CD8^+$) (**k**) in Gl261N4-bearing mice measured by flow cytometry 3 and 7 days post virus injection (dpi). Bar graphs display mean ± SD. For $CD4^+$ T cell infiltration, the *P* values of control vs. OV-Q1 and control vs. OV-CDH1 are $*P = 0.012$, $*P = 0.011$ at 3 dpi and $*P = 0.017$, $**P = 0.007$ at 7 dpi, receptively. The corresponding *P* values for $CD8^+$ T cell infiltration are $*P = 0.038$, $*P = 0.014$ and $*P = 0.025$, $*P = 0.024$. *P* values were generated by one-way ANOVA with Holm's multiple comparisons test ($n = 6$ animals).